Biosensors and Bioelectronics 246 (2024) 115829

Contents lists available at ScienceDirect

Biosensors and Bioelectronics

journal homepage: www.elsevier.com/locate/bios

Improving biosensor accuracy and speed using dynamic signal change and theory-guided deep learning

Junru Zhang [a], Purna Srivatsa [b], Fazel Haq Ahmadzai [a], Yang Liu [a,c], Xuerui Song [a], Anuj Karpatne [b], Zhenyu (James) Kong [a], Blake N. Johnson [a,c,d,e,*]

[a] *Grado Department of Industrial and Systems Engineering, Virginia Tech, Blacksburg, VA, 24061, USA*
[b] *Department of Computer Science, Virginia Tech, Blacksburg, VA, 24061, USA*
[c] *School of Neuroscience, Virginia Tech, Blacksburg, VA, 24061, USA*
[d] *Department of Materials Science and Engineering, Virginia Tech, Blacksburg, VA, 24061, USA*
[e] *Department of Chemical Engineering, Virginia Tech, Blacksburg, VA, 24061, USA*

ARTICLE INFO

Keywords:
Machine learning
Artificial intelligence
False positive
False negative
Reliability
Surface-based biosensor
Cost function supervision

ABSTRACT

False results and time delay are longstanding challenges in biosensing. While classification models and deep learning may provide new opportunities for improving biosensor performance, such as measurement confidence and speed, it remains a challenge to ensure that predictions are explainable and consistent with domain knowledge. Here, we show that consistency of deep learning classification model predictions with domain knowledge in biosensing can be achieved by cost function supervision and enables rapid and accurate biosensing using the biosensor dynamic response. The impact and utility of the methodology were validated by rapid and accurate quantification of microRNA (let-7a) across the nanomolar (nM) to femtomolar (fM) concentration range using the dynamic response of cantilever biosensors. Data augmentation and cost function supervision based on the consistency of model predictions and experimental observations with the theory of surface-based biosensors improved the F1 score, precision, and recall of a recurrent neural network (RNN) classifier by an average of 13.8%. The theory-guided RNN (TGRNN) classifier enabled quantification of target analyte concentration and false results with an average prediction accuracy, precision, and recall of 98.5% using the initial transient or entire dynamic response, which is indicative of high prediction accuracy and low probability of false-negative and false-positive results. Classification scores were used to establish new relationships among biosensor performance characteristics (e.g., measurement confidence) and design parameters (e.g., inputs and hyperparameters of classification models and data acquisition parameters) that may be used for characterizing biosensor performance.

1. Introduction

Barriers to the widespread clinical, industrial, and consumer use of biosensors (Cui et al., 2020; Dervisevic et al., 2020; Iravani, 2020; Khor et al., 2022; Kundu et al., 2019; Tan et al., 2022), which include accuracy, reproducibility, and speed, have motivated the application of deep learning in biosensing. For example, false-positive and false-negative results associated with rapid tests for SARS-CoV-2 were widely publicized during the COVID-19 pandemic (Patel et al., 2023; Un et al., 2021). Also, time delay associated with target analyte binding poses a barrier to rapid and continuous biosensor-based biosurveillance. Recently, several studies showed that trained dogs perform similarly to PCR for the detection of COVID-19, suggesting that artificial intelligence can play a critical role in transforming the speed, accuracy, and reliability of biosensors (Pirrone et al., 2023). Consideration of measurement uncertainty is now being used to define biosensor performance, such as the detection limit (Fonollosa et al., 2014; Lavín et al., 2018).

Deep learning-driven biosensing studies can be broadly classified based on the targeted performance metric (e.g., speed or accuracy), the structure of the biosensor data analyzed (e.g., time-series (TS) or spectral data), and the learning objective (e.g., regression or classification). While deep learning is providing new opportunities in chemical sensing (Cho et al., 2020), such as improving the detection limit, several studies have applied deep learning in biosensing (Ali et al., 2018;

---

* Corresponding author. Grado Department of Industrial and Systems Engineering, Virginia Tech, Blacksburg, VA, 24061, USA.
E-mail address: bnj@vt.edu (B.N. Johnson).

https://doi.org/10.1016/j.bios.2023.115829
Received 17 July 2023; Received in revised form 14 October 2023; Accepted 8 November 2023

Gonzalez-Navarro et al., 2016; Guselnikova et al., 2019; Sagar et al., 2020; Schackart and Yoon, 2021; Wu et al., 2019). For example, Gonzalez-Navarro et al. predicted the amperometric response of a glucose-oxidase biosensor with low error using an artificial neural network (ANN) and observed a nonlinear dependence on glucose concentration, pH, and temperature (Gonzalez-Navarro et al., 2016). Guselnikova et al. used an ANN to identify photoinduced DNA damage and chemical transformations of DNA structure based on spectral data obtained from a label-free surface-enhanced Raman scattering methodology (Guselnikova et al., 2019). Ali et al. classified bacteria with 100% accuracy in training, validation, and test datasets using a nonlinear back propagation neural network (BPNN) with impedance data from a printed biosensor (Ali et al., 2018). Wu et al. presented a high-throughput method that combined particle aggregation-based biosensors with a convolutional neural network (CNN), which enabled rapid detection of herpes simplex virus (HSV) using a biotin-tagged antibody and holographic images (Wu et al., 2019). Sagar et al. demonstrated microglia detection in cell culture using an ANN based on data from a fluorescence lifetime imaging microscopy (FLIM) technique that exhibited a True Positive Rate (TPR) greater than 0.9 (Sagar et al., 2020). While such studies have established the value of using deep learning to improve biosensor performance, various challenges remain, including the creation of explainable deep learning models. A critical review of deep learning-driven biosensing studies (see Table S1) reveals the opportunity to leverage data augmentation and first principles, such as ensuring that the predictions of deep learning models are consistent with domain knowledge in biosensing.

While the majority of deep learning models remain a black box, domain knowledge (e.g., physics) is now being leveraged in several engineering applications of deep learning, including fluid mechanics, materials science, geology, and manufacturing (Bakhshian and Romanak, 2021; Daw et al., 2017; Pawar et al., 2021; Wang et al., 2020; Zhao et al., 2023). The concept of a physics-guided neural network (PGNN) was among the first approaches integrating domain knowledge with deep learning (Daw et al., 2017). In that work, a PGNN was used to predict lake temperature profiles using a physics-guided learning objective, which reduced prediction error by examining prediction consistency with physics. More recently, Zobeiry et al. developed a system of neural networks based on finite element modeling that selected parameters as features to predict material characteristics, including fracture energy and strain-softening parameters (Zobeiry et al., 2020). Pawar et al. proposed a method to guide deep learning models by adding physical parameters in the neural network latent space, including the Reynolds number and predictions from first principles of aerodynamics, which improved the prediction of aerodynamic forces with quantifiable uncertainty (Pawar et al., 2021). Chen et al. created a theory-guided neural network (TGNN) for hard constraint projection (HCP) that ensured the model obeyed a physical mechanism, which improved the efficiency and prediction accuracy relative to an ANN (Chen et al., 2021). Wang et al. presented a novel physics-guided deep learning model to predict tool wear that included physics-data fusion in the pre-processing stage, a physics-based model for extracting information from unlabeled data, and a physics-guided loss function that ensured consistency of predictions with physics (Wang et al., 2020). Zhao et al. introduced a physics-guided deep crystal generative model (PGCGM) for designing crystalline materials that incorporated a physics loss based on atomic position (Zhao et al., 2023). However, theory-guided deep learning has heavily leveraged simulation data and has not yet been leveraged in biosensing applications.

Here, we establish a new methodology for rapid and accurate biosensing based on theory-guided deep learning using the biosensor dynamic response. Consistency of deep learning model predictions with domain knowledge in biosensing is achieved by cost function supervision. The utility and impact of the methodology are demonstrated by a case study on sensitive microRNA (miRNA) detection using the dynamic signal change of cantilever biosensors. We show that data augmentation can address data sparsity and class imbalance challenges that may arise in applying deep learning models to experimental biosensor data (e.g., calibration data). Considering the target analyte concentration as a categorical variable based on the calibration data structure enabled accurate classification of the dynamic biosensor response and, thus, quantification of target analyte concentration and false-negative and false-positive results. We show that the methodology also enables rapid and accurate RNA detection using the biosensor initial transient response, which reduces the time delay of surface-based affinity biosensors, such as those based on antibody- and nucleic acid-based biorecognition elements.

2. Materials and methods

2.1. *MicroRNA detection using DNA-functionalized cantilever biosensors*

The dynamic response, specifically resonant frequency (Δf) vs. time (t), associated with miRNA let-7a (5′ UGAGGUAGUAGGUUGUAUAGUU 3’; 5.4 kDa) detection using DNA-functionalized cantilever biosensors served as the univariate TS data for this study (Johnson and Mutharasan, 2012). Thiolated-DNA probe (HS–C_6-5′ TTTTTTAACTATACAAC 3’; 7.1 kDa) was immobilized on a 1 mm^2 gold pad at the distal tip of the cantilever biosensor by continuous flow of a 3 μM probe solution in a custom flow cell during which Δf was continuously monitored. Following stabilization of the sensor resonant frequency, the remaining Au<111> sites were backfilled with 6-mercapto-1-hexanol at 730 μM in continuous flow. The surface probe immobilization ratio was based on reports and protocols of Rijal et al. (Rijal and Mutharasan, 2007). The data in this study were obtained from five cantilever biosensors that exhibited similar spectral characteristics. Multiple sensors were examined to characterize the batch performance and account for accidental damage that may occur during experimentation (e.g., handling and cleaning). The miRNA detection study in buffer generated 16 dynamic responses that corresponded to the binding response of functionalized biosensors to 16 calibration standards in a continuous-flow detection format. Additional details of biosensor fabrication, functionalization, biorecognition chemistry, measurement format, and data acquisition system are provided in Supporting Information. The quantity and concentration distribution of the standard solutions were selected to align the design of experiments with diagnostic applications, which often yield sparse and imbalanced data (see the Results and Discussion section for additional details). Specifically, the study generated 8, 1, 2, 1, and 4 dynamic responses (i.e., univariate TS) at let-7a concentrations of 1 nM, 100 pM, 10 pM, 1 pM, and 100 fM, respectively.

2.2. *Data pre-processing*

The dynamic biosensor response was transformed using min-max normalization as $\theta(t) = (f(t) - f_i)/(f_f - f_i)$, where f_i is the baseline resonant frequency before target analyte binding, f_f is the baseline resonant frequency after the binding response reached steady state, and $f(t)$ is the continuously monitored resonant frequency. Time $t = 0$ was the start of the binding process (i.e., the biosensor transient response). The normalized dynamic signal change (i.e., biosensor response) contained non-stationary and stationary data associated with the transient binding period and the baseline response after the binding reaction reached a steady state, respectively.

2.3. *Data augmentation*

Jittering, scaling, magnitude warping, window slicing, time warping, and window warping were used for data augmentation (i.e., generating ‘augmented’ dynamic responses) (Iwana and Uchida, 2021; Um et al., 2017). TS data augmentation was performed before normalization (i.e., on the raw signal). A detailed description of the augmentation methods can be found elsewhere (Iwana and Uchida, 2021). Random numbers used in the augmentation techniques were from a normal distribution. The first step of the augmentation process addressed data sparsity, and the second step addressed class imbalance. This process increased the total data size (i.e., the total number of biosensor responses in the dataset) from 16 to 268, which was balanced across the classes. For example, the five class sizes after data augmentation were 56, 55, 50, 55, and 52, which correspond to the target analyte concentrations of 1 nM, 100 pM, 10 pM, 1 pM, and 100 fM, respectively. Additional details associated with the data augmentation process are provided as Supporting Information.

2.4. Classification of dynamic biosensor response using deep learning for quantification of target analyte concentration and likelihood of false results

The dynamic biosensor response was classified based on the target analyte concentration using a recurrent neural network (RNN), which enabled quantification of the target analyte concentration and the likelihood of false-positive and false-negative results. For the unaugmented dataset, the 16 normalized dynamic biosensor responses (i.e., normalized TS data) served as the input to the RNN using a fixed window size (20 points), which generated 2061 time series. For example, one labeled time series with 67 points (time stamps) and a window size of 20 yields $(67 - 20 + 1) = 48$ time series (i.e., sensor signals). Given that the miRNA detection study characterized the biosensor dynamic response to calibration standards at five different concentrations (see Section 2.1), the classification problem included five classes based on the five unique labels (i.e., let-7a concentrations). Thus, the class sizes for the unaugmented dataset after window size processing were 1090, 183, 302, 112, and 374, respectively. The class sizes for the augmented dataset after window size processing were 7630, 10,065, 7550, 6160, and 4862, respectively. The target analyte concentration (i.e., the class associated with the dynamic response) served as the output of the RNN. The RNN contained two hidden layers with 128 neurons per layer and used two prediction components (a forecasting component and a classification component). The prediction component utilized was dependent on the type of loss function used. The forecasting component was created by linking a fully connected layer and the hidden outputs of the RNN with the predicted value using a single output neuron. The classification component was created by connecting the final hidden layer of the RNN to a fully connected layer of output size equal to the number of classes to be predicted (five in this study). *RNN with Cross-entropy (CE) Loss:* The classification component was used. The cost function for classification was binary CE loss associated with the predicted class. *RNN with CE and Mean-Squared-Error (MSE) Losses:* The classification and forecasting components were used. The cost function used for forecasting was MSE loss associated with the forecasted biosensor response. The forecasting and classification components were executed at the same time. The CE and MSE losses associated with the two prediction components (i.e., the classification and forecasting components, respectively) were simultaneously minimized by concurrent training of the forecasting and classification components based on their shared dependence on hidden variables (H).

2.5. Classification of dynamic biosensor response using theory-guided deep learning for quantification of target analyte concentration and likelihood of false results

Theory-guided RNNs (TGRNNs) were created by modifying the aforementioned RNNs based on CE and MSE losses with theory-based losses that reward consistency of the forecasted dynamic response with the theory of surface-based biosensors and observed responses. We use the terminology 'theory-guided' deep learning in this work rather than 'physics-guided' deep learning, since domain knowledge in biosensing includes both physics and chemistry. Theory of surface-based biosensors that employ antibodies or DNA probes (as used here) shows that the concentration of bound target analyte monotonically increases with respect to time (Squires et al., 2008). Thus, a theory-based loss can complement or replace the MSE loss, which is the basis of the RNN forecasting component. *TGRNN with Monotonicity Loss*: The TGRNN with monotonicity loss used the monotonicity loss of Daw et al. (2017), which was calculated using only the forecasted biosensor response of the RNN. Each value (t_i) was compared to its previous value (t_{i-1}) in the forecasted response, and the ReLU function (Nair and Hinton, 2010) was applied to the difference (i.e., t_i - t_{i-1}) to nullify any predictions that followed an increasing monotonic trend (i.e., if the difference exhibited a positive value) and to include a loss for all the cases where monotonicity was violated (i.e., if the difference exhibited a negative value). *TGRNN with Empirical-Monotonicity Loss*: The TGRNN with empirical-monotonicity loss penalized the forecasted biosensor response when increasing monotonicity between the forecasted and observed dynamic biosensor response was violated. The loss was calculated for each window by taking the average ReLU outputs of the difference between the forecasted and observed biosensor response. If the forecasted value was greater than or equal to the observed value, the loss contributed was zero. If the forecasted value was less than the observed value, the loss was non-zero, as calculated by ReLU. *TGRNN with CE and Monotonicity Losses:* This model contained CE and monotonicity losses. To simultaneously minimize the monotonicity and CE losses, the forecasting and classification components were concurrently executed. *TGRNN with CE and Empirical-Monotonicity Losses:* This model contained CE and empirical-monotonicity losses. The empirical-monotonicity and CE losses were simultaneously minimized by concurrently executing the forecasting and classification components. *TGRNN with CE, MSE, and Monotonicity Losses:* This model contained CE, MSE, and monotonicity losses. To simultaneously minimize the CE, MSE, and monotonicity losses, the forecasting and classification components were concurrently executed. *TGRNN with CE, MSE, and Empirical-Monotonicity Losses:* This model contained CE, MSE, and empirical-monotonicity losses. To simultaneously minimize the CE, MSE, and empirical-monotonicity losses, the forecasting and classification components were concurrently executed. *TGRNN Training*: The TGRNNs were trained with 1000 epochs using an Adam optimizer. The training was stopped when the training loss did not improve for 50 successive epochs. *Evaluation of Model Performance:* The performance of the RNNs and TGRNNs was evaluated by the test classification scores (i.e., the F1 score, precision, and recall). The training, validation, and test datasets were obtained using stratified train/test split (i.e., 70%, 15%, and 15% of the data were used for training, validation, and test data, respectively). The stratified split preserved the class distribution. The test data size for the model using unaugmented data was 310 (15% of the data). For models using augmented data, the test data size was 5440 (15% of the data). Stratified train/test split with a fixed random state ensured that the performance using different loss combinations could be compared. The presented classification scores of F1 score, precision, and recall are the averaged values across all classes. The provided scores corresponded to analysis of the test sets unless otherwise specified.

3. Results and Discussion

3.1. Addressing data sparsity and class imbalance in biosensor calibration data via data augmentation

The miRNA detection study using cantilever biosensors involved 16 standard solutions. The cantilever biosensors exhibited resonant frequencies at 19.0 ± 0.1 and 88.4 ± 0.1 kHz, which correspond to the first and second bending modes, respectively. Immersion in liquid caused a decrease in resonant frequency and Q-value of both modes, primarily through an added-mass effect of the surrounding liquid. The first and second resonant frequencies decreased by 4.2 ± 0.7 and 16.2 ± 1.2 kHz ($n = 3$ sensors), respectively. Given its higher mass-change sensitivity, the second mode was used for miRNA detection. Statistical analyses of the biosensor fabrication processes (e.g., variance in biosensor characteristics) and the miRNA detection study are presented in our previous work (Johnson and Mutharasan, 2012). The concentration of the standards, which served as the label for the biosensor responses, ranged from 1 nM to 100 fM, including 100 fM, 1 pM, 10 pM, 100 pM, and 1 nM. The dynamic responses associated with the calibration dataset ranged from 19 to 94 min and contained 67–250 points (pts). The sampling rate varied from 0.24 to 1.02 pt/min. A representative dynamic response for each target analyte concentration is shown in Fig. 1A.

While multiple studies have applied deep learning in medical diagnostic applications, several have employed augmentation of image (Govindaraju et al., 2022) and TS data (Majidov and Whangbo, 2019) before model evaluation. The unaugmented dataset associated with the case study on miRNA detection using cantilever biosensors was sparse and imbalanced. For example, the calibration standard concentrations of 1 nM, 100 pM, 10 pM, 1 pM, and 100 fM had 8, 1, 2, 1, and 4 corresponding TS, respectively. Thus, the dataset exhibited an imbalanced class distribution with more samples located near the upper and lower limits of the dynamic range to synergize with the variation in let-7a concentration across miRNA-based diagnostic assays, which can vary by several orders of magnitude across the nM to sub-fM range depending on the disease or therapeutic approach (Daneshpour et al., 2018; Ouyang et al., 2019; Perron et al., 2007; Simino et al., 2021; Zhang et al., 2017). Biosensor data is often sparse and imbalanced due to measurement and application constraints and may also arise from data management challenges, such as data loss and labeling cost. Several data augmentation methods for TS data were used to address the data sparsity and class imbalance in the calibration data, which expanded the number of labeled dynamic responses from 16 to 268. This approach was consistent with previous studies that have leveraged data augmentation for classification models involving non-biosensing related miRNA applications (Govindaraju et al., 2022; Majidov and Whangbo, 2019), which have used datasets containing 40–200 samples (Duffy et al., 2018; Duy et al., 2016). The class distribution (i.e., samples/class) of the augmented calibration data for concentrations of 1 nM, 100 pM, 10 pM, 1 pM, and 100 fM was 56, 55, 50, 55, and 52, respectively.

Normalized dynamic sensor signal change has been used in several sensing applications, including chemical sensing, biosensing, and electrophysiology. For example, normalized sensor data is extensively used for analysis of EEG and EMG data (Huynh et al., 2020; Jeong et al., 2018; Mohammadi et al., 2015; Niu et al., 2020; Yu et al., 2022). Scaled sensor data (e.g., shifted, normalized, dimensionless), such as TS data, have also been used in chemical sensing and biosensing applications (Irannejad et al., 2013; Mo et al., 2017; Opp et al., 2009; Stoeber et al., 2018; Zhang et al., 2013). A comparison of the unaugmented and augmented normalized biosensor responses in the 10 pM class is shown in Fig. 1B as a representative case. The augmented data captured the trend and features of the experimental univariate TS data. For example, the mean Pearson's correlation score was greater than 0.7 for most samples, indicating that the augmented data represents the experimental data (i.e., the unaugmented dataset).

The decision to normalize the biosensor signal change is also motivated by the traditional approach for quantifying the target analyte concentration using a standard (i.e., calibration) curve. The standard curve for the miRNA detection study using the DNA-functionalized cantilever biosensors was obtained from the net shift in resonant frequency at steady state and the known concentration of target analyte in each solution tested. Specifically, the standard curve is a plot of the net change in resonant frequency (signal change) vs. the target analyte concentration. In this work, the standard curve contained 16 data distributed across the 100 fM – 1 nM concentration range. Linear regression is typically performed on the standard curve data to provide regression scores that can serve as measures of biosensor performance, such as sensitivity (defined as the slope of the regression model) or accuracy, which can be quantified by MSE. As we discussed, such regression scores are useful (e.g., explainable), but classification scores offer predictive power related to false results. Thus, normalization of the dynamic biosensor signal change removes the traditional feature (i.e., biosensor net steady-state signal change) used for quantifying the target analyte concentration from the TS data. This allows the methodology to complement standard curve-based analyses in biosensing and ensures that the predictive power demonstrated through the biosensor dynamic response is not due to the commonly utilized predictive feature. The normalization process also accounts for performance variance among different biosensors, which is a characteristic of batch manufacturing. The error associated with each measurement can be quantified by the sensor noise level. Noise in this study was considered a feature of the signal that may have predictive power and was not removed in data preprocessing. The variance of repeated measurements is often provided as the standard deviation of the net biosensor signal change for different tested calibration standards using the same or different sensors and was reported in our previous work (Johnson and Mutharasan, 2012). Given that biosensor performance is traditionally assessed using linear regression analysis of standard curve data, regression scores are currently utilized to define biosensor performance, such as detection limit, which is related to the slope of the regression model. The correlation coefficient (R^2) is also commonly reported. For example, the standard curve associated with miRNA detection in buffer gave $R^2 = 0.96$ (Johnson and Mutharasan, 2012). While MSE, R^2-adjusted, and R^2-predicted are additional regression metrics for characterizing model fit and predictive power, there remains an opportunity to improve predictions associated with false results using classification models and scores.

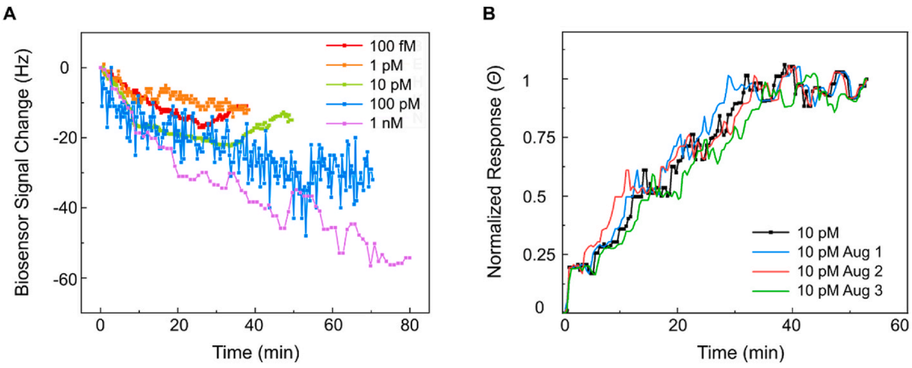

Fig. 1. **A)** Example of the raw dynamic biosensor signal change of a cantilever biosensor during let-7a detection. **B)** Comparison of unaugmented and augmented (Aug) normalized dynamic responses corresponding to detection of let-7a at 10 pM using three augmentation techniques (Aug 1: time warp, Aug 2: window slice, Aug 3: window wrap).

3.2. *Quantifying target analyte concentration and likelihood of false results via classification of dynamic biosensor response using theory-guided deep learning*

While theory-guided feature engineering can potentially improve the performance of non-deep learning models, there is no guarantee that the model predictions ($\hat{Y}$) will be consistent with domain knowledge. Non-deep learning models have the advantage of efficiency (e.g., relatively high speed and reduced computing power), explainability, tuning, interpretation, and utility with relatively fewer data (e.g., unaugmented calibration data), but deep learning offers compelling predictive power for applications that generate abundant data, such as via high-throughput experimentation, simulation, or data augmentation (as leveraged in this study). The creation of explainable deep learning models is an emerging trend in the data science and data-driven STEM communities (Hossain et al., 2020; Huang et al., 2022; Kong and Yu, 2018). Thus, we constructed and examined the performance of a theory-guided recurrent neural network (TGRNN) for miRNA detection that quantifies the target analyte concentration and the likelihood of false-positive and false-negative results.

As shown in Fig. 2A, univariate TS data associated with the normalized dynamic signal change were the input to the neural network. Domain knowledge in biosensing, specifically the monotonicity of surface-based biosensor temporal binding response (Squires et al., 2008), was utilized to modify the cost function through a ‘theory loss.’ Monotonic binding response is a characteristic of surface-based affinity biosensors that employ antibodies and nucleic acid-based biorecognition elements, such as single-stranded DNA used in the miRNA detection case study that generated the data for this work. Previous PGNNs were based on a simple multi-layer perceptron regression model (Daw et al., 2017), but did not employ classification. Here, we created a TGRNN that performs integrated forecasting and classification tasks based on an RNN. An RNN was selected given that dynamic biosensor response is TS data that exhibits temporal correlation. The TGRNN cost

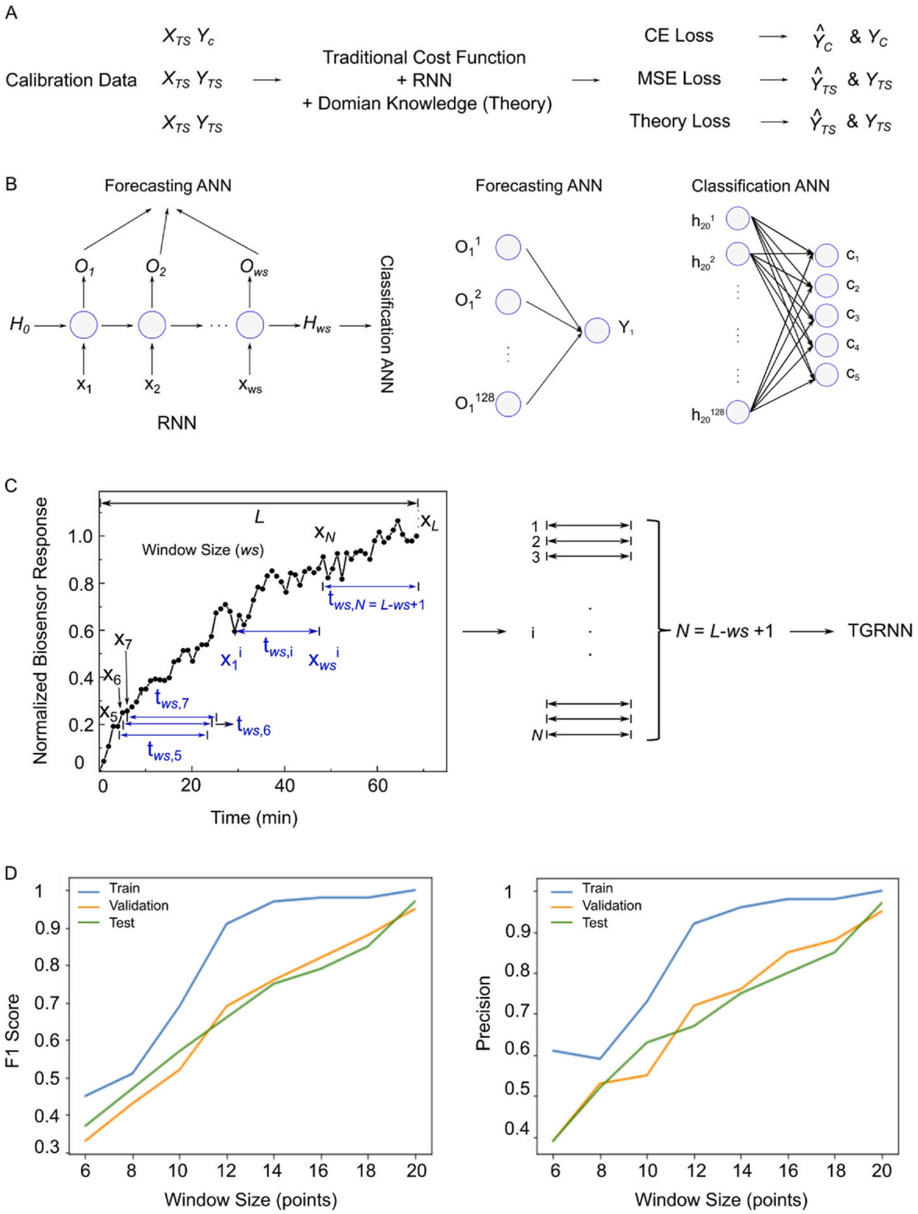

Fig. 2. Schematic of the inputs-outputs **(A)** and structure (i.e., input, final hidden, and output variables) **(B)** of the theory-guided RNN (TGRNN). **C)** Illustration and results of window size (*ws*) hyperparameter tuning. **D**) Effect of window size on the F1 score and precision of the RNN with CE loss (average time for a time window unit increment was 0.24–1.02 min/point).

function contained multiple types of losses: a CE loss, a MSE loss, and two losses associated with the theory of surface-based biosensors. The CE loss was calculated based on the target analyte concentration (Y_c) (i.e., from the classification task). In contrast, the MSE and theory losses were calculated based on TS prediction (Y_{TS}) (i.e., the forecasting task). The TGRNN structure is shown in Fig. 2B. The TGRNN contained many hyperparameters (e.g., the number of layers and neurons per layer), which influenced the feature selection, tuning, and model performance. The TGRNN used in this study contained two hidden layers with 128 neurons per layer. $X_{(0)}$, $X_{(1)}$, …, $X_{(ws)}$ are the sequential values in the TS, which are the inputs to the TGRNN, where the subscript ws stands for window size (i.e., the number of sequential data points input to the model). H and O are the intermediate outputs of the classification and forecasting components, respectively, and represent hidden variables of the TGRNN. $H_{(0)}$, $H_{(1)}$, …, $H_{(ws)}$ are vectors that each contain 128 hidden variables $h^1_{(i)}$, $h^2_{(i)}$, …, $h^{128}_{(i)}$, where the index i ranges from 1 to ws (ws denotes window size). $O_{(0)}$, $O_{(1)}$, …, $O_{(ws)}$ are vectors that each contain 128 hidden variables $o^1_{(i)}$, $o^2_{(i)}$, …, $o^{128}_{(i)}$. Y_i is the output of the TGRNN forecasting component and represents the predicted biosensor response at the next index value in the time series (i.e., t_{ws+1}). The forecasting component is a fully connected layer with an output dimension equal to the window size. The classification component contains a fully connected layer with an output dimension of five, corresponding to the five miRNA concentrations associated with the calibration study. The variables c_1, c_2, c_3, c_4, and c_5 are the outputs of the TGRNN classification component, which represent the predicted miRNA concentration (i.e., 1 nM, 100 pM, 10 pM, 1 pM, and 100 fM, respectively). Motivated by the previous use of a monotonicity loss for PGNN (Daw et al., 2017), we examined the performance of two theory-based losses: 1) a monotonicity loss that examines the consistency of model predictions with theory and 2) an 'empirical-monotonicity' loss that examines the consistency between predictions and observations with theory.

The TGRNN, similar to any neural network, required TS data of consistent length, which were created by discretizing the TS using a moving window. Thus, similar to other neural networks, the window size (ws) was a hyperparameter of the TGRNN. As shown in Fig. 2C, before analysis, the normalized dynamic biosensor signal change, corresponding to a TS of length (L) (i.e., number of points) that varied across the TS data in all classes, was discretized by a fixed window size (ws), generating $N = L - ws + 1$ new TS of $L = ws$, which served as the input to the TGRNN. We note that this process affected the class distribution (balance), given the number of TS generated by the TS discretization process was dependent on the length of the original normalized dynamic biosensor signal change. As a part of hyperparameter tuning, we investigated the effect of window size on the TGRNN performance. Fig. 2D shows the effect of the window size on the performance of the RNN with CE loss in terms of F1 score and precision across the range $ws = 6$ to 20. The train, validation, and test F1 score and precision increased with increasing window size. These results show that the window size, which affects the amount of labeled TS data generated for the model, influences the performance. While a smaller window size increased the data size, the performance (i.e., F1 score and precision) did not improve. Given the results shown in Fig. 2D, all the subsequent TGRNNs in this work used $ws = 20$.

Table S2 shows the TGRNN performance using several loss combinations obtained with the entire dynamic biosensor response for the unaugmented calibration dataset. These results establish a baseline for the performance without data augmentation and demonstrate the value of cost function supervision using domain knowledge in biosensing, specifically a monotonicity loss. Comparison of the TGRNN performance using six different cost functions (i.e., different losses and combinations thereof) revealed that the combination of CE and empirical-monotonicity losses exhibited the best performance based on the classification scores (F1 score, precision, and recall). The F1 score is a weighted measure of model classification capability that accounts for the precision and recall (i.e., the extent of false positives and false negatives) and has been widely used to evaluate the performance of deep learning models for biosensing applications (Cui et al., 2020; Mondal et al., 2023). Precision is a measure of positive predictive value (i.e., false positives), and recall, also known as a true positive rate or sensitivity, is a measure of false negatives. High precision indicates a low number of false positives, and high recall indicates a low number of false negatives. Precision and recall have also been used in the analysis of deep learning models for biosensing applications (Amethiya et al., 2021; Cui et al., 2020; Kim, 2021). The ability to quantify and reduce false results, particularly false negatives, is critical in biosensing applications, such as medical diagnostics and biosurveillance, given the adverse consequences associated with decisions made from false negative results (Bansal et al., 1995; Berkowitz et al., 1990), such as taking no action to a present disease or biothreat. False positive results also have potential adverse consequences, such as those related to quarantine. As shown in Table S2, the test F1 score, precision, and recall using the CE loss were 0.97, 0.98, and 0.97, respectively. The test F1 score, precision, and recall using the CE and MSE losses were all 0.98. The combination of the CE and empirical-monotonicity losses exhibited the best test F1 score, precision, and recall of 0.99. These results suggest that incorporating domain knowledge in biosensing with deep learning models can improve their predictive power.

3.3. Rapid quantification of target analyte concentration and likelihood of false results using the initial transient response

Having demonstrated the TGRNN could accurately quantify target analyte concentration and the likelihood of false results via precision and recall scores, we next examined the ability to reduce the time delay associated with the prediction by using only the initial transient response. As shown in Table S3, the TGRNN also enabled classification of the initial transient response from the unaugmented dataset. These results established a baseline for the performance using the initial transient response without data augmentation and demonstrated the value of integrating domain knowledge for cost function supervision in deep learning-based rapid biosensing applications. For example, the TGRNN with a combination of CE and monotonicity losses exhibited the best performance (test F1 score, precision, and recall were 0.91, 0.92, and 0.91, respectively; see Table S3A).

We next investigated the minimum duration of the initial transient response that enabled accurate and resilient biosensing using the TGRNNs and the effect of data augmentation on performance. The TGRNN performance using the first 15 and 10 min of the initial transient response is shown in Table S3B and C, respectively. As shown in Table S3B, the TGRNN with CE and empirical-monotonicity losses using the first 15 min of the initial transient response gave the best test F1 score and recall of 0.89 and 0.88, respectively. The highest precision was obtained using only the RNN with CE loss. Alternatively, the RNN with CE and MSE losses using the first 10 min of the initial transient response gave the best test F1 score, precision, and recall of 0.6, 0.59, and 0.59, respectively (see Table S3C). The performance using an initial transient period less than 10 min with the unaugmented dataset was not further examined due to the large decrease in performance between 15 and 10 min.

Having examined the performance of the TGRNN with different loss combinations using the entire and initial transient responses from the unaugmented calibration dataset, we next examined the effect of data augmentation on performance. The performance obtained using the entire response and the initial 20, 15, and 10 min of the transient response with the augmented calibration dataset is shown in Table 1A-D, respectively. The training and validation losses are provided in Fig. S1 for 10 min as a representative case, which showed that the model was not overfitting the data based on the similarity of the loss values and trends. The best test precision, recall, and F1 score obtained with the entire biosensor response were 0.93 for TGRNNs with CE and monotonicity losses as well as CE and empirical-monotonicity losses. The best

Table 1

Model performance using the entire biosensor response **(A)** and the first 20 min **(B)**, 15 min **(C)**, and 10 min **(D)** of the initial transient response using augmented biosensor data. Bold black font highlights the best performance, respectively.

A

Model Loss (Augmented Entire Response)	Train			Validation			Test		
	Precision	Recall	F1 score	Precision	Recall	F1 score	Precision	Recall	F1 score
CE	0.84	0.84	0.84	0.82	0.82	0.82	0.81	0.81	0.81
CE & MSE	0.95	0.95	0.95	0.92	0.92	0.92	0.92	0.92	0.92
CE & EMP_MONO	0.96	0.96	0.96	0.94	0.94	0.94	**0.93**	**0.93**	**0.93**
CE & MONO	0.95	0.95	0.95	0.93	0.93	0.93	**0.93**	**0.93**	**0.93**
CE, MSE, & EMP_MONO	0.92	0.92	0.92	0.89	0.89	0.89	0.89	0.89	0.89
CE, MSE, & MONO	0.9	0.9	0.9	0.87	0.87	0.87	0.87	0.87	0.87

B

Model Loss (Augmented 20 min)	**Train**			**Validation**			**Test**		
	Precision	**Recall**	**F1 score**	**Precision**	**Recall**	**F1 score**	**Precision**	**Recall**	**F1 score**
CE	0.99	0.99	0.99	0.97	0.97	0.97	**0.97**	**0.97**	**0.97**
CE & MSE	0.99	0.99	0.99	0.96	0.96	0.96	0.96	0.96	0.96
CE & EMP_MONO	0.99	0.99	0.99	0.97	0.97	0.97	**0.97**	**0.97**	**0.97**
CE & MONO	0.99	0.99	0.99	0.97	0.97	0.97	**0.97**	**0.97**	**0.97**
CE, MSE, & EMP_MONO	0.99	0.99	0.99	0.95	0.95	0.95	0.96	0.96	0.96
CE & MSE, & MONO	0.98	0.98	0.98	0.95	0.95	0.95	0.95	0.95	0.95

C

Model Loss (Augmented 15 min)	**Train**			**Validation**			**Test**		
	Precision	**Recall**	**F1 score**	**Precision**	**Recall**	**F1 score**	**Precision**	**Recall**	**F1 score**
CE	0.99	0.99	0.99	0.97	0.97	0.97	0.97	0.97	0.97
CE & MSE	0.99	0.99	0.99	0.97	0.97	0.97	0.97	0.97	0.97
CE & EMP_MONO	0.99	0.99	0.99	0.97	0.97	0.97	0.96	0.96	0.96
CE & MONO	0.99	0.99	0.99	0.98	0.98	0.98	**0.98**	**0.98**	**0.98**
CE, MSE & EMP_MONO	0.98	0.98	0.98	0.96	0.96	0.96	0.95	0.95	0.95
CE, MSE, & MONO	0.98	0.98	0.98	0.95	0.95	0.95	0.95	0.95	0.95

D

Model Loss (Augmented 10 min)	**Train**			**Validation**			**Test**		
	Precision	**Recall**	**F1 score**	**Precision**	**Recall**	**F1 score**	**Precision**	**Recall**	**F1 score**
CE	1	1	1	0.98	0.98	0.98	0.97	0.97	0.97
CE & MSE	1	1	1	0.98	0.98	0.98	**0.98**	**0.98**	**0.98**
CE & EMP_MONO	1	1	1	0.98	0.98	0.98	0.97	0.97	0.97
CE & MONO	1	1	1	0.98	0.98	0.98	0.96	0.96	0.96
CE, MSE, & EMP_MONO	1	1	1	0.96	0.96	0.96	0.97	0.97	0.97
CE, MSE, & MONO	0.99	0.99	0.99	0.96	0.96	0.96	0.96	0.96	0.96

performance using the first 20 min of the biosensor response with data augmentation was obtained with the RNN with CE loss as well as the TGRNNs with CE and both types of theory losses (test F1 score, precision, and recall = 0.97). With data augmentation, the best performance was obtained using the first 15 and 10 min of the initial transient biosensor response. The best performance using the first 15 min of the initial transient response with data augmentation was obtained using the TGRNN with CE and monotonicity losses (test F1 score, precision, and recall = 0.98). The best performance using the first 10 min of the initial transient response with data augmentation was obtained using the RNN with CE and MSE losses (test F1 score, precision, and recall = 0.98). The TGRNNs with CE and empirical-monotonicity losses as well as CE, MSE, and empirical-monotonicity losses gave comparable performance (0.97). Given that accurate and reliable results were obtained using the first 10 min of the initial transient response, this work shows that theory-guided deep learning can potentially be utilized to significantly reduce the time-to-results (i.e., mitigate the time delay) and false results of surface-based biosensors. We observed that the deep learning models that incorporated multiple (e.g., competing) losses, such as with combined CE, MSE, and theory losses, may lead to fluctuations in the training and validation trends (see Fig. S1). For example, a monotonicity loss is a generalizable theory loss associated with the behavior of functions that describe domain knowledge and can sometimes contradict the characteristics of observed real-world data, which may exhibit signatures associated with experimental sources of measurement uncertainty (e.g., sensor noise). Thus, the performance of the TGRNNs may be potentially further improved by consideration of the theory that drives measurement noise in biosensors (Hassibi et al., 2007). Overall, the results presented in Table 1 demonstrate that data augmentation and theory-guided loss can improve the predictive power of deep learning models using both the entire and initial transient dynamic biosensor response.

As shown in Fig. 3, the performance obtained using the unaugmented experimental data was positively correlated with the data acquisition time (see Fig. 3. A, C, and E). In contrast, as shown in Fig. 3B, D, and F, the performance obtained using data augmentation improved with decreasing data acquisition time, suggesting the ability to perform rapid and accurate biosensing using less than 10 min of the initial transient response. The relationships among classification scores and data acquisition time shown in Fig. 3, which are relations among biosensor performance measures and a design parameter, can define new biosensor performance measures related to biosensor accuracy and reliability. For example, the derivative of the transfer functions (i.e., input-output relations) shown in Fig. 3 can be used to quantify the sensitivity of a biosensor's accuracy to data acquisition time (i.e., detection time). Such relations, in combination with application-dependent performance thresholds (e.g., minimum allowable false-negative results), can potentially help guide biosensor design and characterize biosensor performance.

In this work, the goal was to demonstrate the value of classification

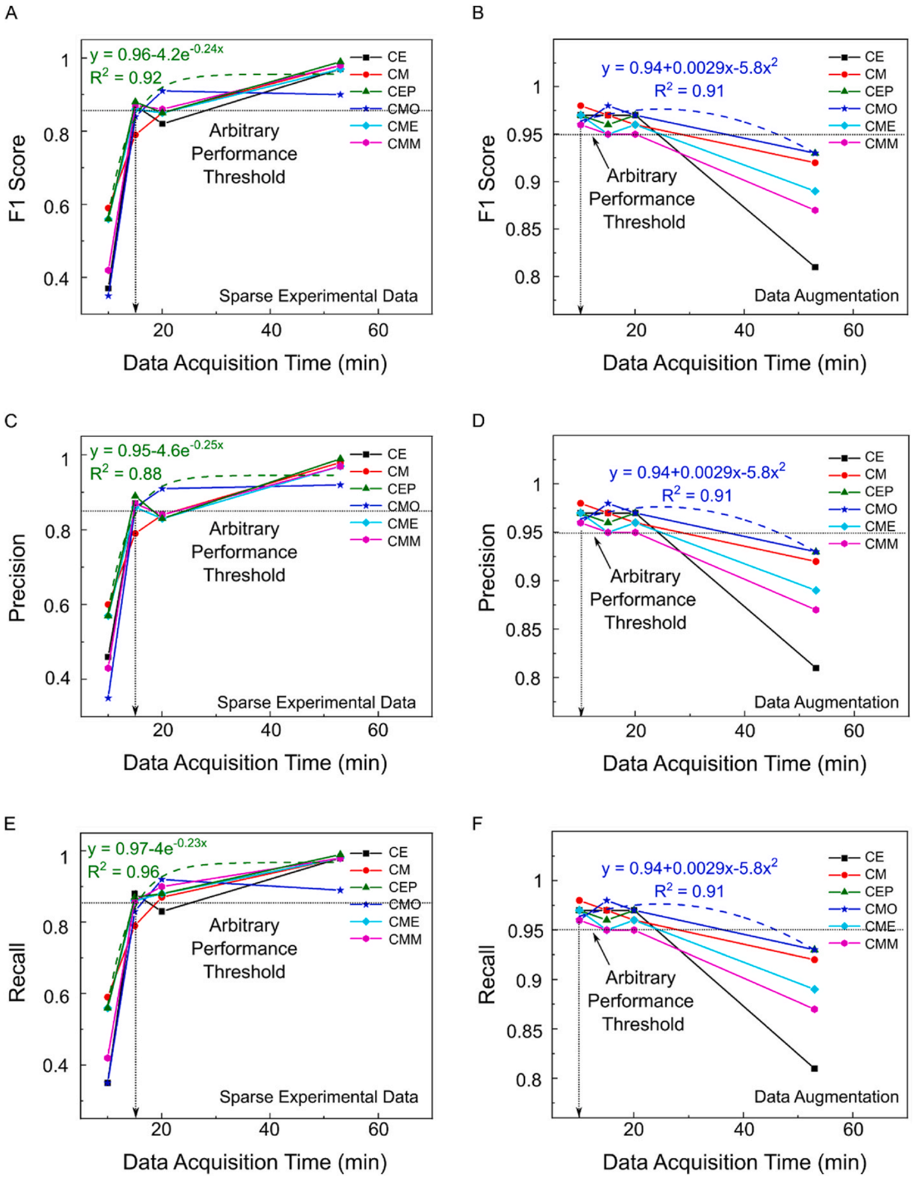

Fig. 3. TGRNN performance comparison for different loss combinations. Comparison of performance using unaugmented (experimental) data in terms of F1 score **(A)**, precision **(C)**, and recall **(E)**. Comparison of performance with data augmentation in terms of F1 score **(B)**, precision **(D)**, and recall **(F)**. *Abbreviations:* Cross-entropy loss (CE); cross-entropy and mean-squared-error losses (CM); cross-entropy and empirical-monotonicity losses (CEP); cross-entropy and monotonicity losses (CMO); cross-entropy, mean-squared-error, and empirical-monotonicity losses (CME); cross-entropy, mean-squared-error, and monotonicity losses (CMM).

scores in biosensing, which are directly related to the extent of false-positive and false-negative results, and the ability to reduce the probability of false predictions (i.e., results) by integrating domain knowledge in biosensing with deep learning. Thus, the focus of this work was methodology development for improving the biosensor performance attributes of accuracy, reliability, and speed using engineering-driven data science models. The structure of our classification problem was constrained by the structure of the input data used and the posed classification problem. Thus, samples below the 100 fM range were not examined. While detection limit improvement was not the focus of this study, using this methodology we were able to quantify how often samples in each class would be properly classified. This methodology may also be used to improve the detection limit if experimental data were obtained (i.e., more samples were tested) from concentrations lower than 100 fM. In future studies, measurements obtained from samples of lower concentration than the detection limit that give net shifts that are statistically insignificant from samples at or near the detection limit of the biosensor would be ideal for improving biosensor detection limit using the proposed method.

4. Conclusions

AI-guided biosensing studies often use deep learning models, such as ANNs, that are agnostic to the theory of processes that drive data generation. Thus, there is no guarantee that predictions are consistent with domain knowledge in biosensing. Here, we demonstrated the ability to improve biosensor performance, specifically to improve accuracy, reduce the likelihood of false results, and reduce biosensor time delay (i.e., data acquisition time), by guiding deep learning models with domain knowledge in biosensing. Consistency of deep learning model predictions with the theory of surface-based biosensors was achieved by cost function supervision using monotonicity constraints. In combination with data augmentation, TGRNNs based on integrated forecasting and multi-class classification tasks were applied to rapid and accurate miRNA quantification. Using the biosensor initial transient response, we also demonstrated the opportunity to leverage theory-guided deep learning to mitigate biosensor time delay. The key contribution of our work lies in demonstrating the value of integrating domain knowledge in data-driven biosensing studies (here, done via cost function supervision of deep learning models), which can further improve biosensor performance, and demonstrating the complementarity of classification models and scores to traditional regression analysis of standard curve data. Our future work will leverage first principles of sensor noise generation for cost function supervision, extend the method to other biosensor data types, examine temporally-dependent losses, involve new classes associated with known false responses, and focus on improving class-wise prediction accuracy based on class-dependent measurement error.

CRediT authorship contribution statement

Junru Zhang: Conceptualization, Data curation, Formal analysis, Investigation, Methodology, Software, Validation, Visualization, Writing – original draft, Preparation, Writing – review & editing. **Purna Srivatsa:** Conceptualization, Data curation, Formal analysis, Investigation, Methodology, Software, Validation, Visualization, Writing – original draft, Preparation, Writing – review & editing. **Fazel Haq Ahmadzai:** Writing – review & editing. **Yang Liu:** Writing – review & editing. **Xuerui Song:** Writing – review & editing. **Anuj Karpatne:** Methodology, Writing – review & editing. **Zhenyu (James) Kong:** Methodology, Writing – review & editing. **Blake N. Johnson:** Conceptualization, Data curation, Formal analysis, Funding acquisition, Investigation, Methodology, Project administration, Resources, Supervision, Validation, Visualization, Writing – original draft, Preparation, Writing – review & editing.

Declaration of competing interest

The authors declare that they have no known competing financial interests or personal relationships that could have appeared to influence the work reported in this paper.

Data availability

Data will be made available on request.

Acknowledgments

BNJ is grateful for the support of the National Science Foundation (CBET-2144310). This work was also supported by GlycoMIP, a National Science Foundation Materials Innovation Platform funded through Cooperative Agreement DMR-1933525.

Appendix A. Supplementary data

Supplementary data to this article can be found online at https://doi.org/10.1016/j.bios.2023.115829.

References

Ali, S., Hassan, A., Hassan, G., Eun, C.-H., Bae, J., Lee, C.H., Kim, I.-J., 2018. Sci. Rep. 8 (1), 1–11.

Amethiya, Y., Pipariya, P., Patel, S., Shah, M., 2021. Intell. Med. 2 (2), 69–81.

Bakhshian, S., Romanak, K., 2021. Environ. Sci. Technol. 55 (22), 15531–15541.

Bansal, R.C., Chandrasekaran, K., Ayala, K., Smith, D.C., 1995. J. Am. Coll. Cardiol. 25 (6), 1393–1401.

Berkowitz, K., Baxi, L., Fox, H.E., 1990. Am. J. Obstet. Gynecol. 163 (3), 975–977.

Chen, Y., Huang, D., Zhang, D., Zeng, J., Wang, N., Zhang, H., Yan, J., 2021. J. Comput. Phys. 445, 110624.

Cho, S.-Y., Lee, Y., Lee, S., Kang, H., Kim, J., Choi, J., Ryu, J., Joo, H., Jung, H.-T., Kim, J., 2020. Anal. Chem. 92 (9), 6529–6537.

Cui, F., Yue, Y., Zhang, Y., Zhang, Z., Zhou, H.S., 2020. ACS Sens. 5 (11), 3346–3364.

Daneshpour, M., Karimi, B., Omidfar, K., 2018. Biosens. Bioelectron. 109, 197–205.

Daw, A., Karpatne, A., Watkins, W., Read, J., Kumar, V. 2017. arXiv preprint arXiv: 1710.11431.

Dervisevic, M., Alba, M., Prieto-Simon, B., Voelcker, N.H., 2020. Nano Today 30, 100828.

Duffy, F.J., Thompson, E., Downing, K., Suliman, S., Mayanja-Kizza, H., Boom, W.H., Thiel, B., Weiner, I.J., Kaufmann, S.H., Dover, D., Tabb, D.L., Dockrell, H.M., Ottenhoff, T.H.M., Tromp, G., Scriba, T.J., Zak, D.E., Walzl, G., 2018. Constortium, GC6-74. Front. Immunol. 9, 661.

Duy, J., Koehler, J.W., Honko, A.N., Schoepp, R.J., Wauquier, N., Gonzalez, J.-P., Pitt, M. L., Mucker, E.M., Johnson, J.C., O'Hearn, A., Bangura, J., Coomber, M., Minogue, T. D., 2016. Sci. Rep. 6 (1), 1–13.

Fonollosa, J., Vergara, A., Huerta, R., Marco, S., 2014. Anal. Chim. Acta 810, 1–9.

Gonzalez-Navarro, F.F., Stilianova-Stoytcheva, M., Renteria-Gutierrez, L., Belanche-Muñoz, L.A., Flores-Rios, B.L., Ibarra-Esquer, J.E., 2016. Sensors 16 (11), 1483.

Govindaraju, H., Sami, M.A., Hassan, U., 2022. IEEE Access 10, 85755–85763.

Guselnikova, O., Trelin, A., Skvortsova, A., Ulbrich, P., Postnikov, P., Pershina, A., Sykora, D., Svorcik, V., Lyutakov, O., 2019. Biosens. Bioelectron. 145, 111718.

Hassibi, A., Vikalo, H., Hajimiri, A., 2007. J. Appl. Phys. 102 (1), 014909.

Hossain, M.S., Muhammad, G., Guizani, N., 2020. IEEE Netw 34 (4), 126–132.

Huang, Z., Li, F., Wang, Z., Wang, Z., 2022. Int. J. Future Comput. Commun. 11 (2), 34–39.

Huynh, P., Warner, G., Lin, H., 2020. J. Adv. Inf. Technol. 11 (1).

Irannejad, R., Tomshine, J.C., Tomshine, J.R., Chevalier, M., Mahoney, J.P., Steyaert, J., Rasmussen, S.G.F., Sunahara, R.K., El-Samad, H., Huang, B., von Zastrow, M., 2013. Nature 495 (7442), 534–538.

Iravani, S., 2020. Mater. Adv. 1 (9), 3092–3103.

Iwana, B.K., Uchida, S., 2021. PLoS One 16 (7), e0254841.

Jeong, D.K., Yoo, S., Jang, Y., 2018. In: Proceedings of the 24th ACM Symposium on Virtual Reality Software and Technology. Association for Computing Machinery, Tokyo, Japan. Article 134.

Johnson, B.N., Mutharasan, R., 2012. Anal. Chem. 84 (23), 10426–10436.

Khor, S.M., Choi, J., Won, P., Ko, S.H., 2022. Nanomaterials 12 (2), 221.

Kim, M.-J., 2021. Biosensors 11 (7), 228.

Kong, Y., Yu, T., 2018. Sci. Rep. 8 (1), 16477.

Kundu, M., Krishnan, P., Kotnala, R.K., Sumana, G., 2019. Trends Food Sci. Technol. 88, 157–178.

Lavín, Á., Vicente, J., Holgado, M., Laguna, M.F., Casquel, R., Santamaría, B., Maigler, M. V., Hernández, A.L., Ramírez, Y., 2018. Sensors 18 (7), 2038.

Majidov, I., Whangbo, T., 2019. Sensors 19 (7), 1736.

Mo, G.C.H., Ross, B., Hertel, F., Manna, P., Yang, X., Greenwald, E., Booth, C., Plummer, A.M., Tenner, B., Chen, Z., Wang, Y., Kennedy, E.J., Cole, P.A., Fleming, K. G., Palmer, A., Jimenez, R., Xiao, J., Dedecker, P., Zhang, J., 2017. Nat. Methods 14 (4), 427–434.

Mohammadi, M., Al-Azab, F., Raahemi, B., Richards, G., Jaworska, N., Smith, D., de la Salle, S., Blier, P., Knott, V., 2015. BMC Med. Inf. Decis. Making 15 (1), 108.

Mondal, H.S., Ahmed, K.A., Birbilis, N., Hossain, M.Z., 2023. Sci. Rep. 13 (1), 3742.

Nair, V., Hinton, G.E., 2010. Rectified linear units improve restricted Boltzmann machines. In: Proceedings of the 27th International Conference on Machine Learning (ICML-10), pp. 807–814.

Niu, J., Tang, Y., Sun, Z., Zhang, W., 2020. IEEE J. Biomed. Health Inform. 24 (5), 1321–1332.

Opp, D., Wafula, B., Lim, J., Huang, E., Lo, J.-C., Lo, C.-M., 2009. Biosens. Bioelectron. 24 (8), 2625–2629.

Ouyang, T., Liu, Z., Han, Z., Ge, Q., 2019. Anal. Chem. 91 (5), 3179–3186.

Patel, S.K., Surve, J., Parmar, J., Ahmed, K., Bui, F.M., Al-Zahrani, F.A., 2023. IEEE Rev. Biomed.Eng. 16, 22–37.

Pawar, S., San, O., Aksoylu, B., Rasheed, A., Kvamsdal, T., 2021. Phys. Fluids 33 (1), 011701.

Perron, M.P., Boissonneault, V., Gobeil, L.-A., Ouellet, D.L., Provost, P., 2007. Regulatory RNAs. In: Sioud, M. (Ed.), Target Discovery and Validation Reviews and Protocols: Volume 2: Emerging Molecular Targets and Treatment Options. Humana Press, Totowa, NJ, pp. 311–326.

Pirrone, F., Piotti, P., Galli, M., Gasparri, R., La Spina, A., Spaggiari, L., Albertini, M., 2023. Sci. Rep. 13 (1), 3679.

Rijal, K., Mutharasan, R., 2007. Anal. Chem. 79 (19), 7392–7400.

Sagar, M.A.K., Cheng, K.P., Ouellette, J.N., Williams, J.C., Watters, J.J., Eliceiri, K.W., 2020. Front. Neurosci. 14, 931.

Schackart, K.E., Yoon, J.-Y., 2021. Sensors 21 (16), 5519.

Simino, L.A.P., Panzarin, C., Fontana, M.F., de Fante, T., Geraldo, M.V., Ignácio-Souza, L. M., Milanski, M., Torsoni, M.A., Ross, M.G., Desai, M., Torsoni, A.S., 2021. Sci. Rep. 11 (1), 8980.

Squires, T.M., Messinger, R.J., Manalis, S.R., 2008. Nat. Biotechnol. 26 (4), 417–426.

Stoeber, M., Jullié, D., Lobingier, B.T., Laeremans, T., Steyaert, J., Schiller, P.W., Manglik, A., von Zastrow, M., 2018. e965 Neuron 98 (5), 963–976.

Tan, M., Xu, Y., Gao, Z., Yuan, T., Liu, Q., Yang, R., Zhang, B., Peng, L., 2022. Adv. Mater. 34 (27), 2108491.

Um, T.T., Pfister, F.M., Pichler, D., Endo, S., Lang, M., Hirche, S., Fietzek, U., Kulić, D., 2017. Data augmentation of wearable sensor data for Parkinson's disease monitoring using convolutional neural networks. In: Paper Presented at the Proceedings of the 19th ACM International Conference on Multimodal Interaction.

Un, K.-C., Wong, C.-K., Lau, Y.-M., Lee, J.C.-Y., Tam, F.C.-C., Lai, W.-H., Chen, H., Winowo, S., Zhang, X., Yan, M., Wu, E., Chan, S.-C., Lee, S.-M., Chow, A., Tong, R.C.-F., Majmudar, M.D., Rajput, K.S., Hung, I.F.-N., Siu, C.-W., 2021. Sci. Rep. 11 (1), 4388.

Wang, J., Li, Y., Zhao, R., Gao, R.X., 2020. J. Manuf. Syst. 57, 298–310.

Wu, Y., Ray, A., Wei, Q., Feizi, A., Tong, X., Chen, E., Luo, Y., Ozcan, A., 2019. ACS Photonics 6 (2), 294–301.

Yu, Z., Chen, J., Liu, Y., Chen, Y., Wang, T., Nowak, R., Lv, Z., 2022. IEEE J. Biomed. Health Inform. 26 (10), 4987–4995.

Zhang, K., Wang, K., Zhu, X., Xie, M., 2017. Anal. Chim. Acta 949, 53–58.

Zhang, L., Tian, F., Liu, S., Dang, L., Peng, X., Yin, X., 2013. Sensor. Actuator. B Chem. 182, 71–79.

Zhao, Y., Siriwardane, E.M.D., Wu, Z., Fu, N., Al-Fahdi, M., Hu, M., Hu, J., 2023. npj Comput. Mater. 9 (1), 38.

Zobeiry, N., Reiner, J., Vaziri, R., 2020. Compos. Struct. 246, 112407.